

Research Article

Dielectric Properties of PbNb_2O_6 up to 700°C from Impedance Spectroscopy

Kriti Ranjan Sahu¹ and Udayan De²

¹ Physics Department, Egra SSB College, Egra, Purba Medinipur, West Bengal 721429, India

² Kendriya Vihar, C-4/60, V.I.P. Road, Kolkata 700052, India

Correspondence should be addressed to Udayan De; ude2006@gmail.com

Received 28 January 2013; Revised 28 March 2013; Accepted 29 March 2013

Academic Editor: Iwan Kityk

Copyright © 2013 K. R. Sahu and U. De. This is an open access article distributed under the Creative Commons Attribution License, which permits unrestricted use, distribution, and reproduction in any medium, provided the original work is properly cited.

Piezoelectric materials have wide band gap and no inversion symmetry. Only the orthorhombic phase of lead metaniobate (PbNb_2O_6) can be ferroelectric and piezoelectric below Curie temperature, but not the rhombohedral phase. High temperature piezoelectric applications in current decades have revived international interest in orthorhombic PbNb_2O_6 , synthesis of which in pure form is difficult and not well documented. Second problem is that its impedance spectroscopy (IS) data analysis is still incomplete. Present work attempts to fill up these two gaps. Presently found synthesis parameters yield purely orthorhombic PbNb_2O_6 , as checked by X-ray Rietveld analysis and TEM. Present 20 Hz to 5.5 MHz IS from room temperature to 700°C shows its ferroelectric Curie temperature to be one of the highest reported, $>574^\circ\text{C}$ for 0.5 kHz and $>580^\circ\text{C}$ for 5.5 MHz. Dielectric characteristics and electrical properties (like capacitance, resistance and relaxation time of the equivalent CR circuit, AC and DC conductivities, and related activation energies), as derived here from a complete analysis of the IS data, are more extensive than what has yet been reported in the literature. All the properties show sharp changes across the Curie temperature. The temperature dependence of activation energies corresponding to AC and DC conductivities has been reexamined.

1. Introduction

A generator of pressure or movement or ultrasonic wave and their sensor/detector can be fabricated utilizing inverse and direct piezoelectric effect, respectively. These possibilities opened up a huge array [1] of medical, industrial, and other applications of piezoelectric materials with significant commercial implications. Commercial piezoelectric materials have mostly been barium titanate (BT), lead zirconate titanate (PZT), or materials based on BT or PZT. But Curie temperature (T_c), the upper limit for piezoelectricity, is at best 130°C [2] for BT and 365°C for a modified PZT. So, higher T_c materials are being developed worldwide for high temperature (HT) applications. Lead metaniobate (PbNb_2O_6), shortened here as PNO, with a higher Curie temperature (517 to 570°C in different papers), is one of the present candidate materials [2–14]. It was discovered [3] in 1953. However, synthesis of its piezoelectric phase, the metastable orthorhombic structure, in a pure state is difficult [4]. During the preparation of the orthorhombic PNO by quenching

from a temperature above 1250°C , a few competing compounds and phases (like the rhombohedral PNO phase) tend to form. The rhombohedral PNO is not piezoelectric. In fact, the difficulty [4] of forming single-phase and high-density orthorhombic PNO, together with the success of BT, PZT, and related piezomaterials for near room temperature applications, somewhat halted R & D on PNO after the initial years of pioneering work and publications [5–9]. In the meantime, a need has developed for high temperature (HT) piezoelectric materials (i) for HT ultrasonic imaging of nuclear fuel rods through molten metal coolants [15] in Fast Breeder Reactors and (ii) for HT applications like sensors in car exhaust systems. So, since the late nineties, work on PNO has been revived by a few groups (Table 1) in search of higher Curie temperature materials. The stable forms of PbNb_2O_6 are rhombohedral (at low temperature) and tetragonal (at high temperature). Quenching from the tetragonal form, as mentioned earlier, leads to metastable orthorhombic form at room temperature. Roth showed by X-ray diffraction

[5, 6] that the orthorhombic PNO (ferroelectric) changes to a tetragonal structure (paraelectric) above $\sim 570^\circ\text{C}$.

Goodman [3] had earlier concluded the $T_{(\text{Curie})}$ of quenched PNO to be 570°C , from their dilatometric and dielectric characterizations. Although this temperature is regarded even in recent papers [10] as the Curie temperature of PbNb_2O_6 , almost all the recent electrical measurements have obtained much lower values of its Curie temperature (Table 1). Reference [10] quoted $T_{(\text{Curie})}$ of 500°C for Ferroperm (Denmark) PNO samples (1995) and 495°C for Morgan Matroc (UK) PNO samples (1997). Lower $T_{(\text{Curie})}$ in these commercial samples may or may not be due to efforts to optimize other piezoelectric parameters. Table 1 has been compiled from recent publications. It shows $T_{(\text{Curie})}$ to be in the range 517°C to 540°C only, except in present samples. So, there is a need to optimize preparation conditions of quenched PbNb_2O_6 to get highest possible Curie temperature, high purity and high density. A pointer in this direction is our observation on quenched PNO [11] of an endothermic signal at 570.6°C in Differential Scanning Calorimetry [12].

Here, our preparation of high quality orthorhombic PNO and results of our impedance spectroscopy up to 700°C and over a wide frequency range from 20 Hz to 5.5 MHz, with a detailed analysis, have been presented. Intrinsic cationic defects in niobates like LiNbO_3 and their role are well known [16]. Likely lattice defects in a quench-prepared PbNb_2O_6 sample should similarly be regarded as an intrinsic part of the sample. The structure of the samples has, therefore, been characterized fully before other studies. Although some work on PNO (Table 1) and a few on various targeted chemical substitutions in PNO have been reported in the literature, not all possible dielectric and electrical parameters for PNO itself have yet been derived from IS data. This has been attempted here. The dielectric response in such an electroceramic is known to be complex with many contributions that need to be known and understood. So, desirable observations like the highest $T_{(\text{Curie})}$ as well as all uncommon observations of the present work are reproduced. All possible data analysis has been carried out, yielding important parameters like bulk resistance, relaxation times, activation energies, AC and DC conductivity, and phase angle.

2. Materials and Methods

Aldrich lead(II) oxide (PbO , 99.999%, yellowish orange and Melting Point = 886°C) and niobium pentoxide (99.9% GR) of Loba Chemie, weighed in proper proportion to give $\text{Pb}:\text{Nb}=1:2$, plus 2% of excess PbO , have been well ground under isopropyl alcohol, dried, and pelletized. Additions of excess PbO were introduced by some earlier workers to compensate possible evaporative loss of PbO . To get best PbNb_2O_6 , present firings have been done in stages at 1050°C , 1290°C and 1270°C in a box furnace with PID temperature controller. Extra PbO (3%) has been added before the 3rd firing. All our firings have been done in palletized form to provide intimate contact and reduce Pb loss. But grinding and repalletizing at each step have also been undertaken, to improve mixing and the sample quality. After the last

TABLE 1: Comparison of recently reported Curie temperatures of orthorhombic PbNb_2O_6 samples.

Sample	Sintering		Curie temperature $T_{(\text{Curie})}$ in $^\circ\text{C}$
	Temp. ($^\circ\text{C}$)	Time (h)	
Present	1270	4.5	$T_{(\text{Curie})} > 576$ for 4.0 MHz, and > 574 for 0.5 kHz.
[17]	1270	4.5	517
[18]	1270	—	534 and 540 (both at 10 kHz)
[19]	—	—	540 (presumably at 80 kHz)
[20]	1240–1260	4	530 (at 10 kHz)
[13]	1270	4.5	531 (at 1 kHz), 528 (at 1 MHz) and 533 (at 10 MHz)

firing, the samples have been quenched. The samples have been characterized by XRD with Rietveld analysis [11] and Transmission Electron Microscopy (TEM).

The impedance spectroscopy has been carried out using Solatron “SI 1260 Impedance Gain Phase Analyzer” with a high temperature attachment. Our PNO pellets (diameter ~ 12 mm and 2.2 to 2.4 mm thick) have not been poled before measurement. Silver paint coat on the flat faces of the pellet under study served as the electrodes for IS measurements. This measurement of ϵ' and ϵ'' (the real and imaginary components, respectively, of the relative dielectric constant i.e., permittivity) has been done for different measuring frequencies at different values the sample temperature (T) while heating from room temperature to 700°C .

3. Results and Discussion

XRD pattern and Rietveld analysis [11], Figure 1(a), confirmed the orthorhombic structure and absence of any other phase. The smallness of the difference of the fitted graph and raw data proved our Rietveld fit to be good. It yields $a = 17.6468(7) \text{ \AA}$, $b = 17.9512(7) \text{ \AA}$, and $c = 3.8704(1) \text{ \AA}$. The samples showed about 80% of the theoretical density on average. TEM diffractograms [6] with the electron beam on individual grains of the ceramic sample always gave diffraction patterns that matched these lattice parameters from XRD result. One TEM diffraction pattern is shown in Figure 1(b). This way, all of the nearly forty grains examined have been found to be in orthorhombic phase.

Figures 2–4 show ϵ' versus frequency, ϵ'' versus frequency, and $\tan \delta = \epsilon''/\epsilon'$ versus frequency results (over 20 Hz to 5.5 MHz range) for 12 temperatures from 50°C to 700°C . In Figure 2, real part (ϵ') of dielectric constant decreases with increase of measuring frequency up to about $\ln f = 12$ to 14 region, implying ~ 162 kHz to ~ 1203 kHz region, and then increases sharply with increase of frequency as reported earlier [13] for all temperatures except at low temperatures like 200°C . Moreover, ϵ' is low and less dependent on frequency at low temperatures up to 300°C , leading to overlap of several graphs. It increases with increase of temperature, up to 573°C . Graph of ϵ' shows significantly increased values in the 573°C graphs with respect to

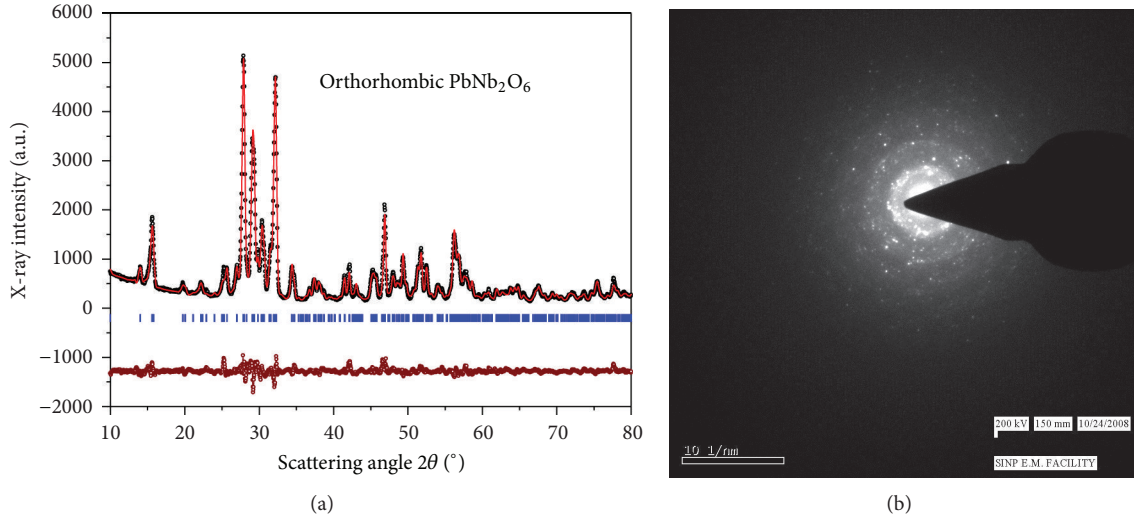


FIGURE 1: (a) Rietveld fit (red graph) to XRD data points (black circles) for orthorhombic PbNb_2O_6 with their difference shown by the continuous curve in the smaller-sized graph. The vertical blue bars below the main graph are the calculated peak positions. (b) Electron diffraction pattern for HR Transmission Electron Microscopy on a selected grain (microcrystal) of quenched lead metaniobate (PNO).

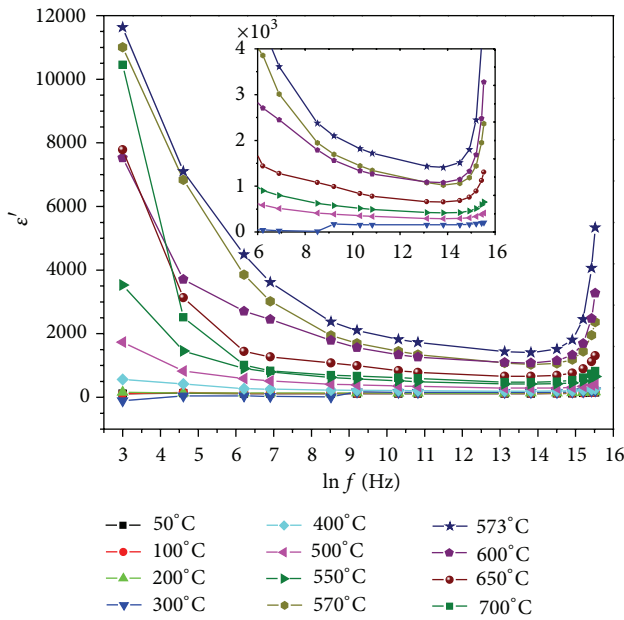


FIGURE 2: Frequency dependence of the real part of dielectric constant (ϵ') in the frequency range 20 Hz ($\ln f = 2.995$) to 5.5 MHz ($\ln f = 15.52$), compiled from heating runs at different temperatures for quenched PNO sample, the orthorhombic phase of PbNb_2O_6 . The inset is an enlarged view of the variation of ϵ' in the higher frequency range.

the 570°C graph. This temperature is the region of ferroelectric to paraelectric phase transition, as is clearer in graph on temperature variation (Figure 5). One must note the interesting decrease of ϵ' with further increase of temperature above 573°C. This, in fact, shows up in ϵ' versus T plot as peaking at around 573°C. Here, it was studied up to 700°C. The values at different temperatures of dielectric dispersion with respect to

frequency, which will be proportional to $d\epsilon'/d(\ln f)$, will be discussed from the low frequency, specifically $\ln f$ (Hz) < 7, part of Figure 2. At a low temperature of 100°C, $d\epsilon'/d(\ln f) = 2.483 \pm 0.739$ only, increasing to 41.158 ± 7.805 at 300°C, whereas at the high temperature of 573°C, $d\epsilon'/d(\ln f) = -4121.578 \pm 226.784$, a high value.

In Figure 3, frequency dependence of ϵ'' or the imaginary part of relative permittivity is more at low frequencies and higher temperatures, the ϵ'' versus frequency graph for 700°C being at top in the lower frequency region. Here, ϵ'' decreases steeply as frequency increases from 20 Hz to about $\ln f = 8$ implying $f = 2.98$ kHz. A weak peaking of ϵ'' at $\ln f = 13.8$, implying $f = 984.6$ kHz, is visible for graphs for low temperatures like 50°C, 300°C, 500°C, and 550°C in the enlarged view. Our higher temperature graphs show no peak in this temperature region but only a slow increase of ϵ'' to allow peaking at higher frequencies. This fall and peaking of ϵ'' has been shown and discussed by earlier workers [13], although the details differ. Dielectric loss ($\tan \delta$) in Figure 4 approximately follows ϵ'' with respect to frequency and temperature dependence.

Figures 5 and 6 are plots with respect to temperature, of ϵ' and $\tan \delta = \epsilon''/\epsilon'$, respectively. The peak value of ϵ' is denoted by ϵ'_{\max} and its position on the temperature axis by T_m . Data for eight frequencies, selected out of 20 Hz to 5.5 MHz data in Figures 2–4, have been plotted in Figures 5 and 6 to avoid overlaps and provide a clearer view of the graphs.

Fall of ϵ' and, hence, of the dielectric susceptibility, $\chi' = (\epsilon' - 1)$, with increasing T , a characteristic of the paraelectric phase and exhibited here for $T > T_m$ region, is due to opposition of the increasing thermal agitation, to dipole alignment. The rise of ϵ' with T in the $T < T_m$ region is believed to be achieved by the increase in the number of dipoles available for alignment [21]. Sharpness of the peak at T_m indicates near absence of diffused scattering in present samples, as discussed elaborately later. Let a minor peculiarity

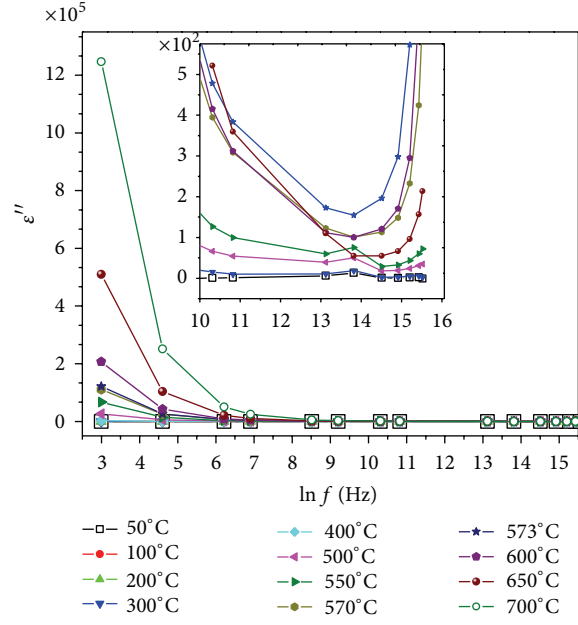


FIGURE 3: Frequency dependence of the imaginary part (ϵ'') of dielectric constant in the frequency range 20 Hz to 5.5 MHz, compiled from heating runs at different temperatures, for quenched PNO sample, the orthorhombic phase of PbNb_2O_6 . The inset is an enlarged view of the variation of ϵ'' in the higher frequency range.

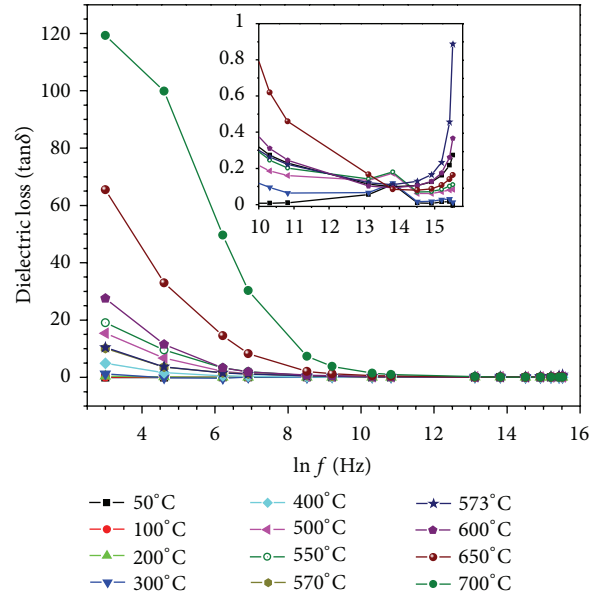


FIGURE 4: Frequency dependence of the dielectric loss ($\tan \delta$) in the frequency range 20 Hz to 5.5 MHz, compiled from heating runs at different temperatures, for quenched PNO sample, the orthorhombic phase of PbNb_2O_6 .

be discussed first. A wide minimum (Figure 5), appearing at 300°C, for frequencies 0.5 kHz, 1 kHz, and 5 kHz in ϵ' versus T , as well as in $\tan \delta$ versus T graph (Figure 6), cannot be readily explained. However, the more important feature of this work is the large permittivity peak at T_m with T_m ranging from 574°C to 576°C as the measurement frequency is increased from 0.5 kHz to 4 MHz, as mentioned earlier. In Figure 7, the peak value, ϵ'_{\max} , of ϵ' shows a sharp fall initially and then a slow rise with increase of measuring

frequency. The value of ϵ'_{\max} decreases from 11623 to 1450 as the frequency (f) increases from 20 Hz to 1 MHz. Then, for $f > 1$ MHz, the value of ϵ'_{\max} increases slowly, being about 5465 at 5.5 MHz. The prominent peak of the imaginary part ϵ'' in the ϵ'' versus T graph can be seen to be around T_m as expected. The dielectric loss ($\tan \delta$) also peaks at around T_m .

Above T_m , ϵ' decreases with increase of T , and, hence, the material is obviously paraelectric above T_m . It is ferroelectric below T_m . This transition temperature gives [22] the Curie

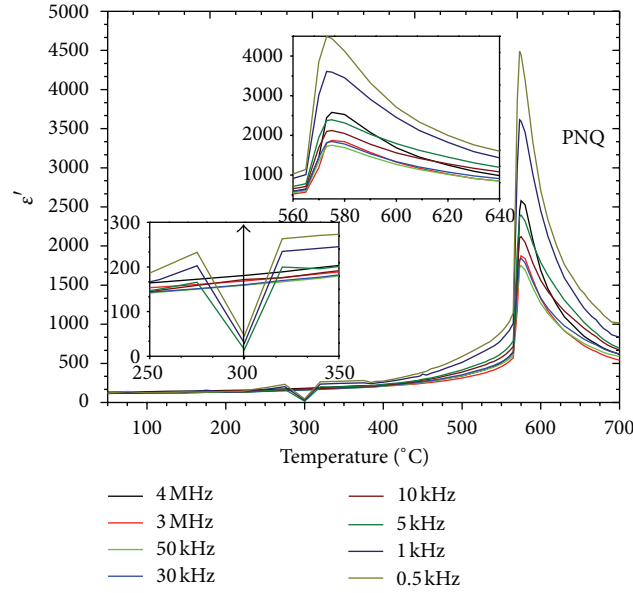


FIGURE 5: Temperature dependence of the real part (ϵ') of dielectric constant in the temperature range of 50°C to 700°C, at different frequencies, for quenched PNO sample, the orthorhombic phase of PbNb_2O_6 .

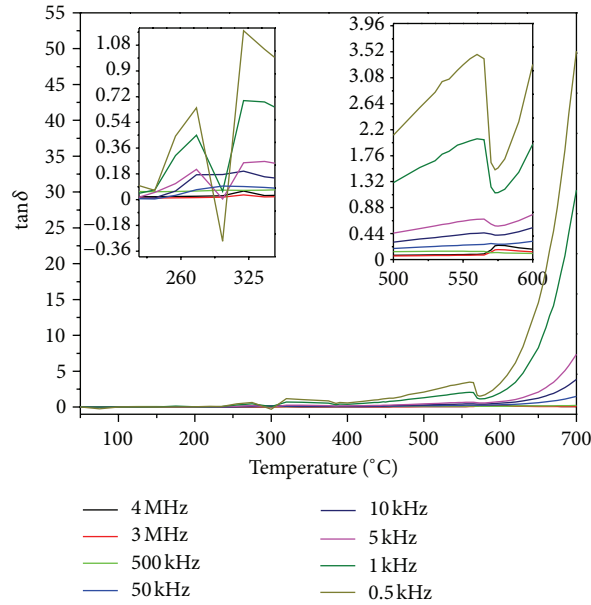


FIGURE 6: Temperature dependence of the dielectric loss ($\tan \delta$) in the range 50°C to 700°C at different frequencies for quenched PNO sample, the orthorhombic phase of PbNb_2O_6 . Two insets magnify two important features.

temperature. So, present impedance spectroscopy measurements indicate a high Curie temperature that depends on frequency, 576°C for 4.0 MHz and 580°C for 5.5 MHz, for example.

The plot of Z'' (imaginary part of the impedance) versus Z' (real part of the impedance), called Nyquist diagram [23], is based on the well-known Cole-Cole plot of ϵ'' versus ϵ' . The Z'' versus Z' plot for our orthorhombic PNO is shown in Figures 8(a) and 8(b). The straight line segments joining of the data points in Figures 8(a) and 8(b) are drawn only as

a guide to the eye. Single semicircular nature of the plots is clearer in the higher temperature plots, as the lower temperature plots, like that for 200°C in the insert of Figure 8(a), show a near linear rise, possible for a large semicircle. An important observation is that the Nyquist diagram here shows only one semicircular arc [23] over the studied frequency range 20 Hz to 5.5 MHz. One semicircle implies only one contribution, here from the sample grains and not from any second source (e.g., grain boundaries or electrode effect). A sample with one semicircle Nyquist diagram or Cole-Cole plot is equivalent

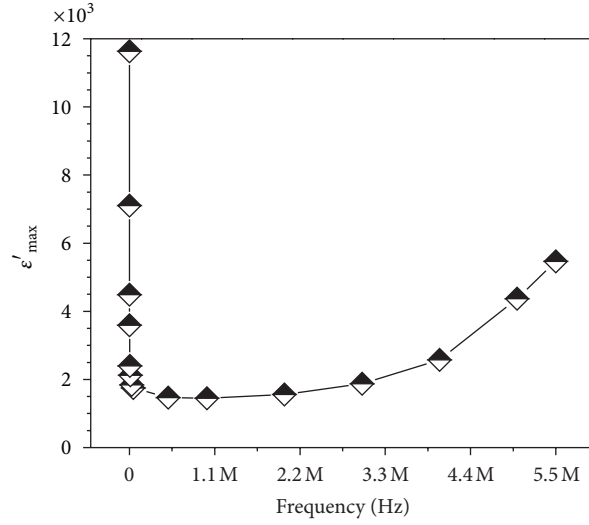


FIGURE 7: The maximum value (ϵ'_{\max}) of the real part of dielectric constant in the in the temperature range of 50°C to 700°C, as a function of frequency (Hz), for quenched PNO sample, the orthorhombic phase of PbNb_2O_6 .

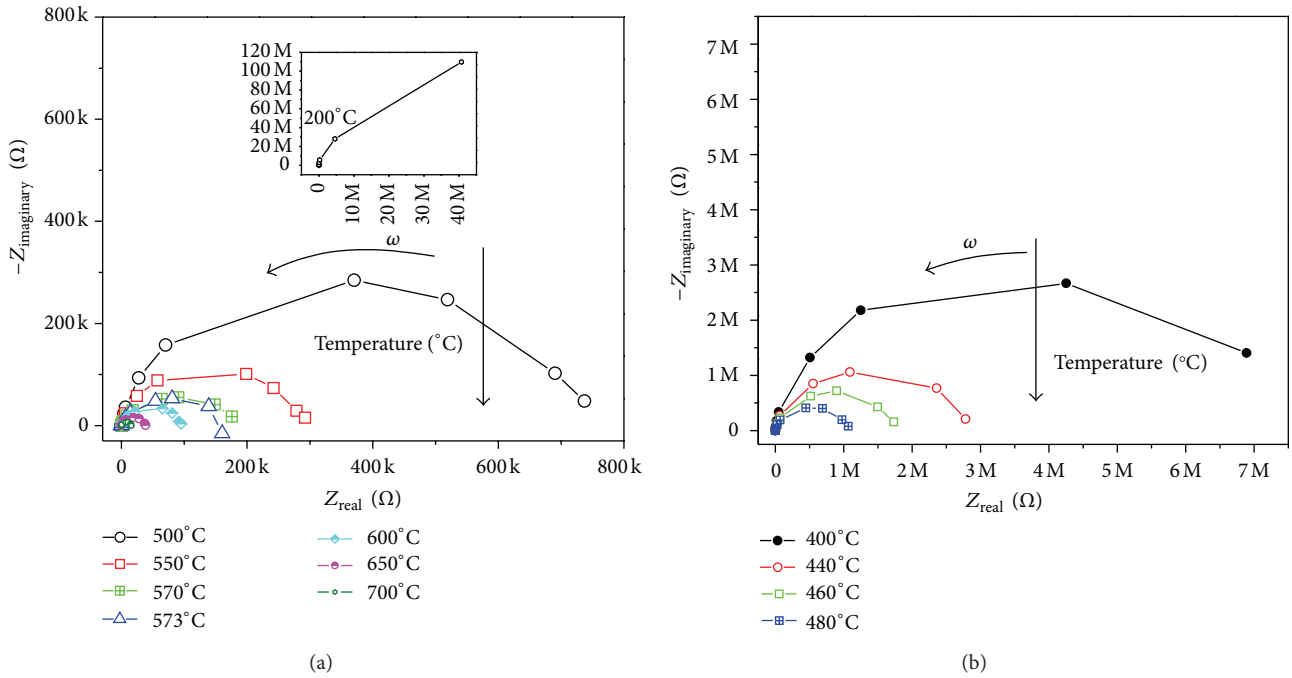


FIGURE 8: (a) Plot of the imaginary part, $Z_{\text{imaginary}}$ in ohm, of impedance versus its real part, Z_{real} in ohm, for quenched PNO sample, PbNb_2O_6 in orthorhombic phase, at temperatures: 500°C, 550°C, 570°C, 573°C, 600°C, 650°C, and 700°C. Since the complex impedance $Z^* = Z_{\text{real}} - jZ_{\text{imaginary}}$, quantity $(-Z_{\text{imaginary}})$ has actually been plotted in the figure. (b) Plot of the imaginary part, $Z_{\text{imaginary}}$ in ohm, of impedance versus its real part, Z_{real} in ohm, for the quenched PNO sample, PbNb_2O_6 in orthorhombic phase, at temperatures: 400°C, 440°C, 460°C, and 480°C. Since the complex impedance $Z^* = Z_{\text{real}} - jZ_{\text{imaginary}}$, quantity $(-Z_{\text{imaginary}})$ has actually been plotted in the figure.

[23] to a bulk resistance R and a capacitance C in parallel. These elements give rise to a time constant $\tau = CR$, the dielectric relaxation time of the basic material. The frequency ω_m of the peak of the Nyquist diagram can find the relaxation time τ as $(\omega_m)(\tau) = 1$ for this peak point [23]. At this point, Z'' has its maximum value. So, many authors [24, 25] use the frequency of peak (i.e., maximum) of Z'' versus frequency plot to find the relaxation time τ .

Present work additionally suggests an alternative method (based [23] on $Z'' = R/2 = Z'/2$ criterion) of determining relaxation time (τ). We later compare the two methods, with the finding that they match (Figure 14) fairly well, match being better at higher temperatures. Often the centre of the semicircular arc of the Nyquist diagram is not on the Z' -axis, so that the semicircle is seen to be depressed by an angle (θ) below the Z' -axis. This is the case, if there is a distribution

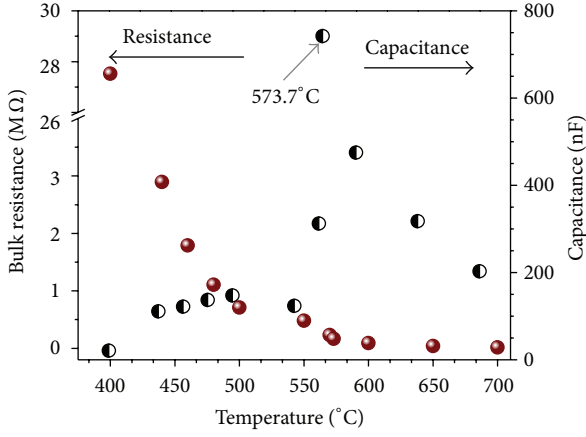


FIGURE 9: Bulk resistance R in $M\Omega$ and capacitance C in nF of the equivalent RC circuit of quenched $PbNb_2O_6$ sample, plotted against temperature, T . Here, R and C have been calculated from Nyquist diagram of Z' and Z'' in 20 Hz to 5.5 MHz range and the corresponding time constant $\tau = CR$, related to the dielectric relaxation time.

of relaxation times. This θ is determined by the width of the distribution of relaxation time.

If the semicircle starts near the origin at $Z' = R_\infty$ and intercepts the Z' -axis again at R_0 , $R = (R_0 - R_\infty)$ gives [23] the bulk resistance. Fitting the impedance spectroscopy (Z'' versus Z') data, usually forming an arch, to the equation of a circle, its radius r and θ and, hence, R_0 can be determined. Bulk resistance $R = (R_0 - R_\infty) = 2r \cdot \cos \theta$ has thus been calculated from our data in Figure 8 and plotted in Figure 9. It is found that the semicircle of data points for a particular temperature in Figures 8(a) and 8(b) reduces in size with increase of temperature, implying smaller bulk resistance of the sample at higher temperatures as documented in Figure 9. Real part ϵ' of permittivity in present samples in the paraelectric region has been fitted to the modified Curie-Weiss law [26], $(1/\epsilon' - 1/\epsilon'_{\max}) = (T - T_m)\gamma/C_w$, where C_w is Curie-Weiss constant and γ is the diffusivity parameter with $1 < \gamma < 2$. For a ferroelectric relaxor, γ is at its highest value of 2.

The previous equation reduces to Curie-Weiss law for $\gamma = 1$. The full equation can be rewritten as $\ln(1/\epsilon' - 1/\epsilon'_{\max}) = \gamma \ln(T - T_m) - \ln C_w$. So, plotting of $\ln(1/\epsilon' - 1/\epsilon'_{\max})$ versus $\ln(T - T_m)$ for different frequencies, as shown in Figures 10(a) and 10(b), gives the fit parameters (Table 2). Present finding that γ is nearly 1 in all cases proves that the relaxor property is minimum for these samples. This $\gamma = 1$ leads to the observed sharpness of the peak at T_m . Relaxor piezoelectric materials, on the other hand, show a broadened peak.

Next, AC conductivity (σ_{ac}) has been calculated from the dielectric loss ($\tan \delta$) data using the empirical formula, $\sigma_{ac} = \omega \epsilon_0 \epsilon' \tan \delta = 2\pi f \epsilon_0 \epsilon''$, where $\epsilon_0 = 10^7/4\pi c^2 = 8.845 \times 10^{-12} \text{ F}\cdot\text{m}^{-1}$ = vacuum permittivity and c = speed of light in vacuum. Figure 11 presents this result on AC conductivity as a function of $1000/T$. Now the maxima in different graphs of Figure 11 (prominent only in high frequency graphs) are at $1000/T \sim 1.18 \text{ K}^{-1}$, that is, at $T \sim 573^\circ\text{C}$ that corresponds

TABLE 2: Result of fitting ϵ versus T data to the modified Curie-Weiss equation, as detailed in the text.

Frequency (Hz)	T_m ($^\circ\text{C}$)	$C_w \times 10^5$ ($^\circ\text{C}$)	γ	ϵ'_{\max}
5.5 M	579.5 ± 4	2.187	1.141	5472.6
3.0 M	575.2 ± 2	1.739	1.136	1876.1
2.0 M	574.8 ± 1	1.471	1.110	1574.2
50 k	574.9 ± 1	1.236	1.035	1752.2
1.0 k	573.8 ± 1	5.237	1.283	3613.9
0.5 k	573.0 ± 1	2.635	1.117	3632.5
0.1 k	572.5 ± 1	0.877	0.744	7103.5

to the ferroelectric-to-paraelectric transition. AC activation energy (E_{ac}) was calculated using the empirical Arrhenius relation $\sigma_{ac} = \sigma_0 \exp(-E_{ac}/kT)$.

The aforementioned maximum, known to occur in the AC conductivity graph at around the ferroelectric-paraelectric phase transition temperature (T_c), is due to domain reorientation, domain wall motion, and the dipolar behavior [27]. In our data in Figure 11, there are three distinct temperature regions of Arrhenius type conduction, (a) ~ 50 to $\sim 300^\circ\text{C}$ section, corresponding to [28] electron or hole hopping, (b) ~ 400 to $\sim 550^\circ\text{C}$ part, due to conduction by small polarons and oxygen vacancies, and (c) ~ 580 to $\sim 700^\circ\text{C}$ high temperature region due to intrinsic ionic conduction [29]. Data in these three regions have been separately fitted to the Arrhenius relation as shown in Figure 12. The slope of $\ln(\sigma_{ac})$ versus $1/T$ plot gives AC activation energy E_{ac} .

The previous fitting avoided the region between 300 and 400°C , as it showed an unexplained peak. However, the rise in some graphs at $\sim 300^\circ\text{C}$ to $\sim 322^\circ\text{C}$ region of Figure 11 reminds one of the anomaly at $\sim 300^\circ\text{C}$ in ϵ'' versus T as well as in $\tan \delta$ versus T graphs in Figures 5 and 6. It is noteworthy that temperature dependence of σ_{ac} is radically different below and above this temperature zone, indicating different AC activation energies for AC conduction. However, somewhat wavy nature of the data at low frequencies and low temperatures, in this and other work [30], and suggestion of the rise by only one point in high frequency graphs prevent definite conclusions on the rise. These data at low frequencies (here 0.5, 1, and 10 kHz in Figure 11) and low temperature ($T < 401^\circ\text{C}$) have not been considered for present AC activation energy calculation in next paragraph. In the high temperature graph in Figure 12, E_{ac} falls rapidly with increase of measuring frequency up to 500 kHz and then becomes weakly dependent on frequency at higher frequencies. The low temperature graph of E_{ac} is practically independent of frequency over the range (500 kHz to 5 MHz) studied here. As seen in the graphs, the AC activation energy is higher at lower frequencies, 0.5 kHz data giving 0.954 eV (with $\sigma_0 = 57.56 \Omega\cdot\text{m}^{-1}$) for 400 to 550°C , and 1.17 eV (with $\sigma_0 = 1.508 \times 10^3 \Omega\cdot\text{m}^{-1}$) for 580 to 700°C . These values fall to 0.523 eV (with $\sigma_0 = 24.62 \Omega\cdot\text{m}^{-1}$) for 400 to 550°C and -1.994 eV (with $\sigma_0 = 6.253 \times 10^{-13} \Omega\cdot\text{m}^{-1}$) for 580 to 700°C , that is, in paraelectric region, respectively. Figure 13 gives the variation of $Z_{\text{real}} = Z'$ and $Z_{\text{imaginary}} = Z''$ against the measuring frequency. Here, Z' and Z'' graphs are seen to merge in

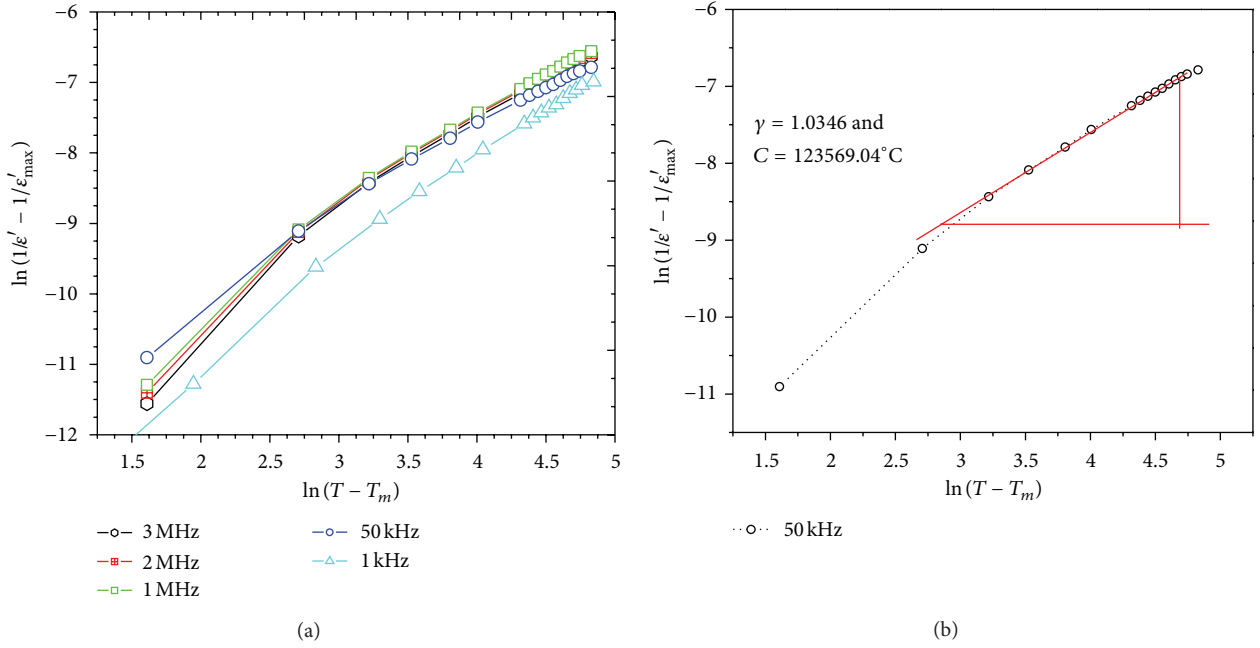


FIGURE 10: (a) Plot of $\ln(1/\epsilon' - 1/\epsilon'_{\max})$ versus $\ln(T - T_m)$ for quenched PNO sample, the orthorhombic phase of PbNb_2O_6 , at various frequencies (3 MHz, 2 MHz, 1 MHz, 50 kHz, and 1 kHz). It examines the relationship, expected for the paraelectric phase of a normal ferroelectric. (b) A specific example of finding the parameters ($\gamma = 1.0346$ and $C = 123569.04^\circ\text{C}$) of the modified Curie-Weiss law from the 50 kHz plot of $\ln(1/\epsilon' - 1/\epsilon'_{\max})$ versus $\ln(T - T_m)$ for the paraelectric phase of quenched PbNb_2O_6 , which is orthorhombic.

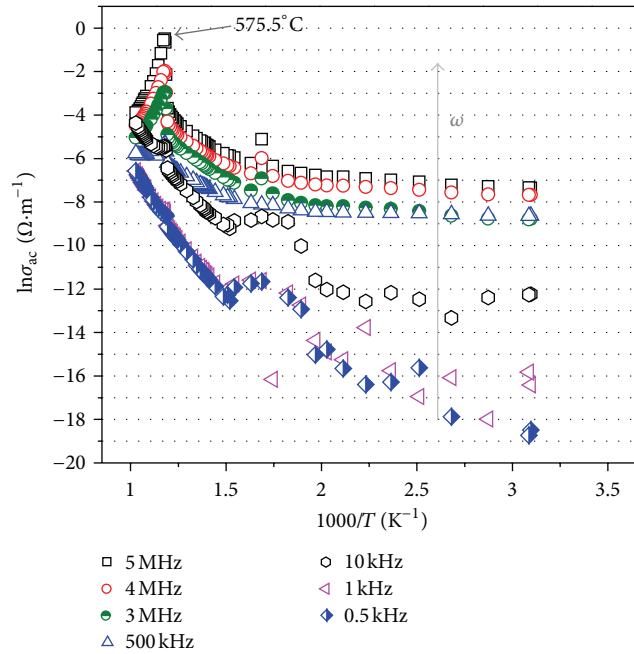


FIGURE 11: Frequency dependence of AC conductivity in the temperature range 50°C to 700°C , at different frequencies, for quenched PNO sample, the orthorhombic phase of PbNb_2O_6 .

the high frequency region approaching zero value. The single semicircular Cole-Cole plot suggests an equivalent circuit [23] of resistance R and capacitance C in parallel giving the well-known complex impedance $Z^* = R/(1 + j\omega RC) = Z' - jZ''$. Applying the relation $\tau = CR$ and the earlier-mentioned

condition: $\omega_m\tau = 1$, one gets $Z'' = R/2$ and $Z' = R/2$. So, relaxation time related frequency is the frequency at which Z' versus frequency and Z'' versus frequency graphs cross each other making $Z' = Z''$. We calculate this relaxation time and present it as the relaxation time τ_{cross} in Figure 14.

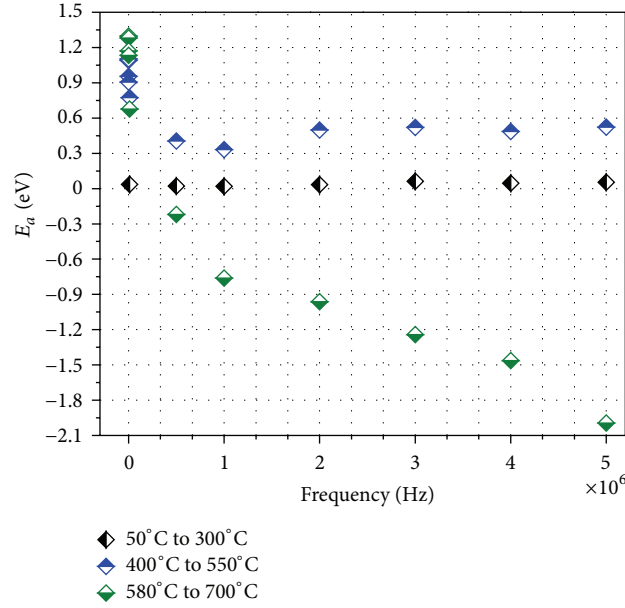


FIGURE 12: AC conductivity activation energy, E_a , as calculated from the slope of the Arrhenius plot of $\ln(\sigma_{ac})$ versus $1/T$, resulting in three E_a values for three temperature ranges. This figure depicts the variation of E_a with measuring frequency.

We determine relaxation time also from the frequency at the Z'' peak of Z'' versus frequency graphs (Figure 13) as done by others [30], calling it τ_{peak} to compare it in Figure 14 with τ_{cross} . Figure 14 shows that τ_{cross} and τ_{peak} behave similarly proving correctness of each approach. But these two graphs show different values with more relative scatter in the τ_{peak} graph. This point shows up again in DC conductivity discussion in next paragraphs.

The decrease of relaxation time with temperature has been adequately discussed in the literature [31]. Relaxation time for this material is seen to fall with increasing temperature, except for a prominent peaking at the ferroelectric to paraelectric transition temperature. $R = (R_0 - R_\infty) \sim R_0$, since $R_\infty \ll R_0$. This R has already been calculated from Figure 8. So, presently determined $CR = \tau$ value gives us C . These two equivalent circuit parameters C and R have been presented in Figure 9. Here, there is an impressive peaking of capacitance C at the Curie temperature. Another related parameter, the angle (θ), has been plotted against temperature in Figure 15. Clearly, it may be positive or negative, depending on the position of the centre of the semicircular arc. Variation of the impedance phase angle, $\delta = \tan^{-1} - (Z'/Z'')$, with frequency, plotted on a logarithmic scale, is called Bode plot [23, 26]. Bode plots at different temperatures have been shown in Figures 16(a) and 16(b), graphs for 570°C, 573°C, and 600°C being given in Figure 16(b) to avoid overlap. At low frequencies and high temperatures (e.g., the 700°C graph), the constant phase part of the phase angle can be seen to be predominating. For a pure capacitor, $\delta = -90^\circ$, while for a resistor it is zero. For a capacitor, the voltage, V_c , lags behind the response current by 90° . In the phase angle plot, an approach to pure capacitive behavior at low frequency values can usually be identified by $\delta \rightarrow -90^\circ$. For an RC circuit, it will have an intermediate value and depends on

ω as seen in the graph. Figure 16(b) contains data sets at T_m region temperatures and shows a prominent increase of the phase angle between 1 MHz and 5.5 MHz. The frequency ranges for near constancy of the phase angle (e.g., over 20 Hz to ~ 1 kHz for 700°C) can be observed from the figures. This constant phase region appears at low frequencies for the high temperature runs and at high frequencies for low temperature runs.

DC conductivity has been calculated using the relation [32], $\sigma_{dc} = (\epsilon_0 \epsilon_\infty)/\tau$ from experimentally found τ and $\epsilon_\infty (= \epsilon'$ value as $f \rightarrow \infty$). Using τ_{cross} and τ_{peak} data, as found in Figure 14, temperature dependence of $\sigma_{dc}(cross)$ and $\sigma_{dc}(peak)$, and, hence, that of two sets of DC activation energy have been calculated for the present PNO samples. Result from each technique shows expected increase of σ_{dc} with temperature (T), as shown in Figure 17. DC activation energy (E_{dc}) due to DC conductivity [14] was calculated using the empirical Arrhenius relation $\sigma_{dc} = \sigma_0 \exp(-E_{dc}/kT)$, where k is Boltzmann constant, σ_0 is preexponential factor and E_{dc} is the DC activation energy for the conduction process [33–36], by plotting $\ln(\sigma_{dc})$ versus $1/T$. Figure 19 gives this DC activation energy for different temperature ranges, indicated by the horizontal bars, as found independently from τ_{cross} and τ_{peak} data, for two- and three-region fits. Almost all earlier authors determined DC activation energy, E_{dc} , from relaxation time via DC conductivity. The 2-segment fit has been utilized in the literature for the usual τ_{peak} -based evaluation of E_{dc} below and above $T_{(Curie)}$.

Gonzalez et al [36] calculated relaxation times ($\tau = \tau_{CC}, \tau_T, \tau^*$) and other parameters for PNO sample from their 450°C to 590°C measurement of the temperature dependence of the imaginary dielectric modulus, separately by frequency domain analysis and by time domain analysis. Their τ^* ,

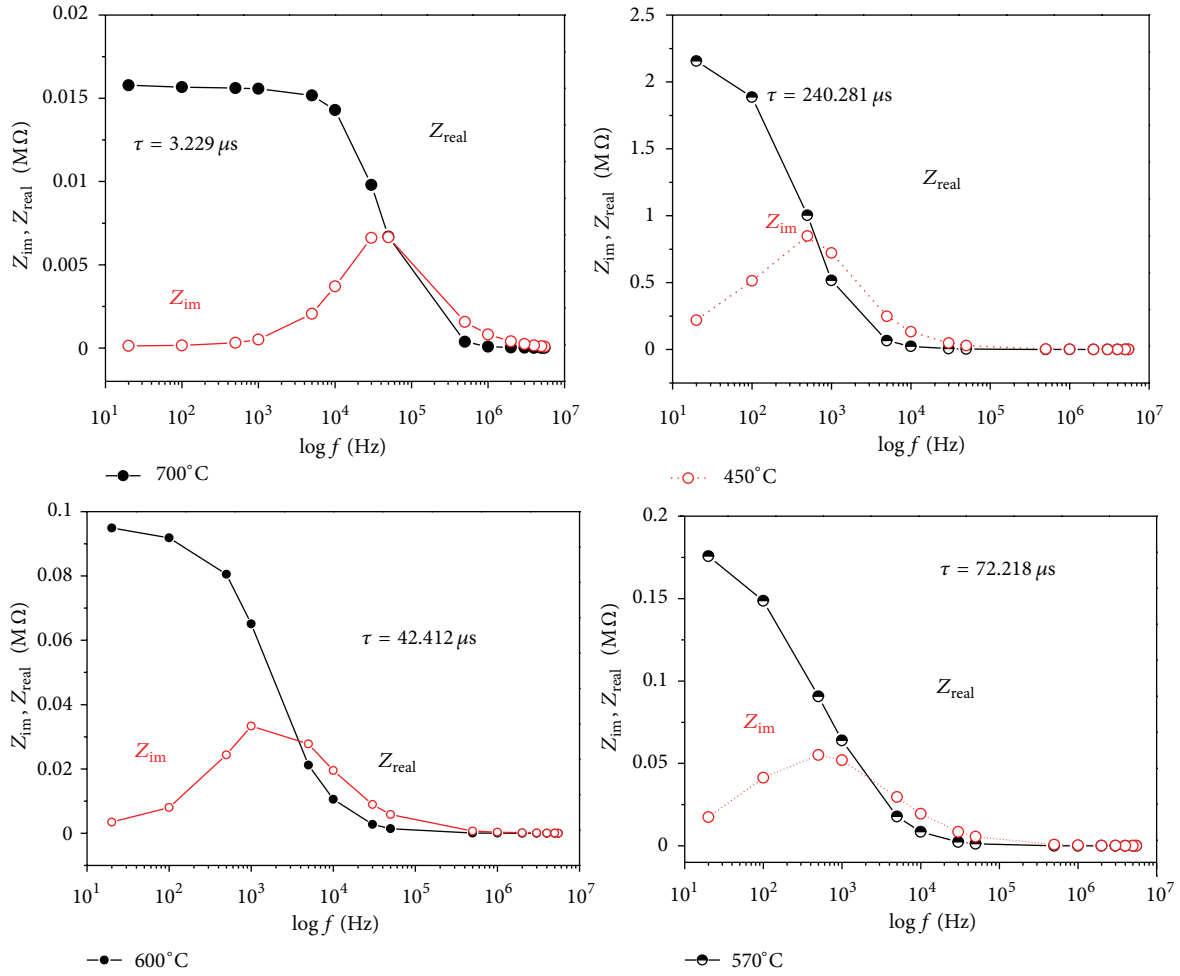


FIGURE 13: Variation of Z_{real} (real part of impedance) and Z_{im} (imaginary part of impedance) with frequency (plotted in log scale) at different temperatures. Frequency at the intersection of the two graphs gives a value of the relaxation time of the system, to be called τ_{cross} . Relaxation time estimated from the frequency) at the peaking in Z'' is to be called τ_{peak} .

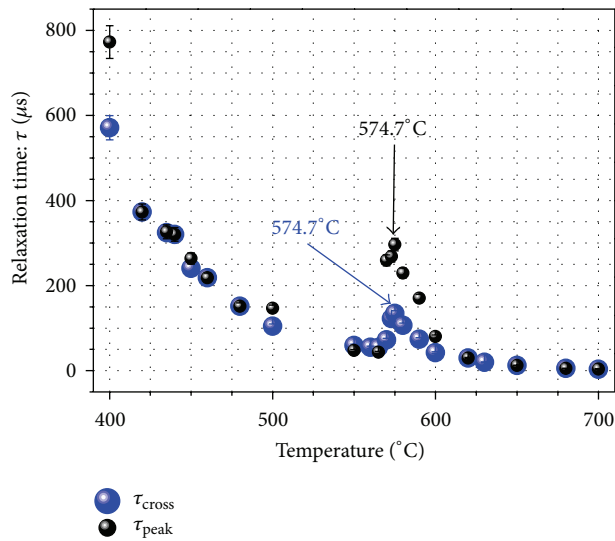


FIGURE 14: Variation of the relaxation time (τ_{peak} and τ_{cross}) with temperature (T) has been shown in one graph, relaxation times τ_{peak} and τ_{cross} being estimated by two different techniques as defined in Figure 13.

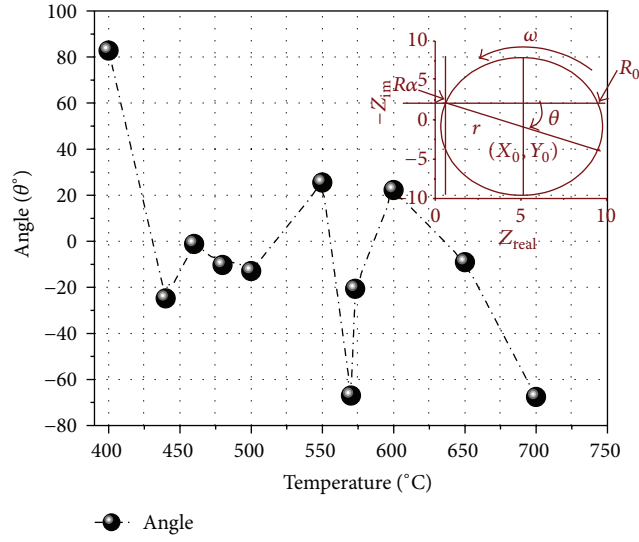


FIGURE 15: Diagrammatic definition of the angle (θ) of Nyquist Plot (in the inset), as detailed in the text, and its variation with temperature.

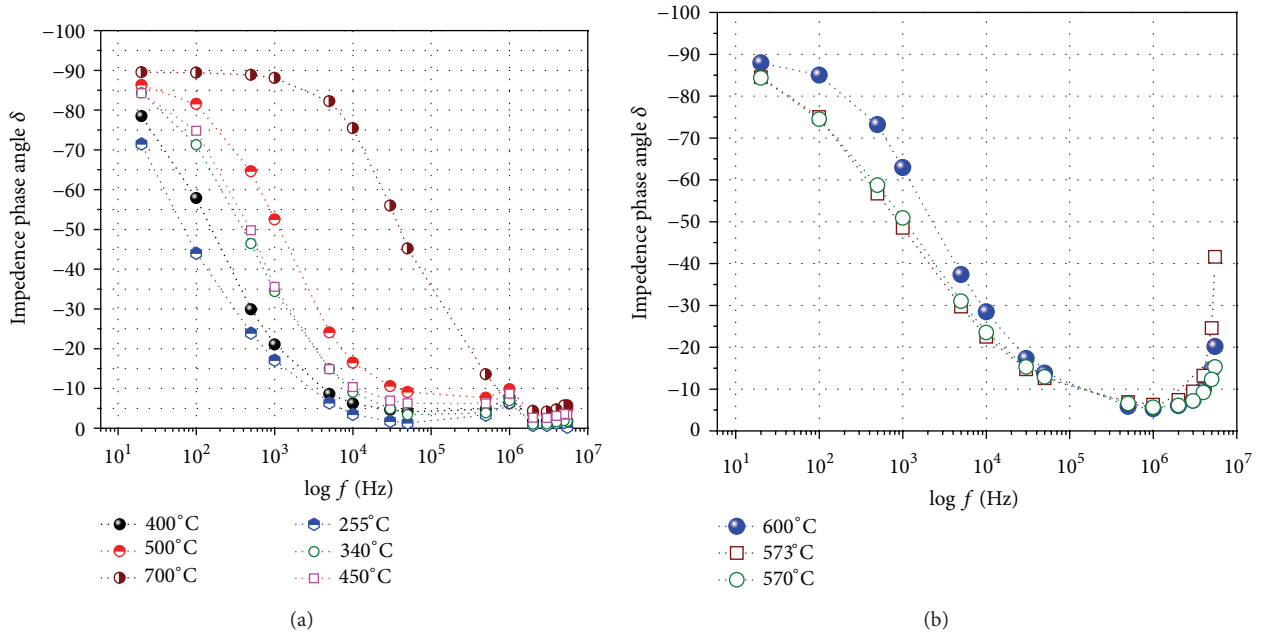


FIGURE 16: (a) Variation of the impedance phase angle, $\delta = \tan^{-1} - (Z_{\text{real}}/Z_{\text{im}})$, with frequency at different temperatures (255°C, 340°C, 400°C, 450°C, 500°C, and 700°C). (b) Variation of the impedance phase angle, $\delta = \tan^{-1} - (Z_{\text{real}}/Z_{\text{im}})$, with frequency at a few important temperatures (570°C, 573°C, and 600°C).

relaxation time due to thermal effect, was calculated in time domain using the Kohlrausch-Williams-Watts function, $f(t) = e^{-(t/\tau^*)^\beta}$. Finally $\langle \tau_T \rangle$, the average relaxation time, was calculated using the relation, $\langle \tau_T \rangle = (\Gamma(1/\beta)/\beta)\tau^*$, where Γ is the Euler gamma function. Next, σ_{dc} was calculated using the relation $\sigma_{\text{dc}} = \epsilon_{\text{oo}}/\langle \tau_T \rangle$. They made separate liner fits to their $\ln(\sigma_{\text{dc}})$ versus $1/T$ data for data below $T_{\text{(Curie)}}$ and for data above $T_{\text{(Curie)}}$, finding, however, similar values $E_{\text{dc}} = 1.08$ eV below $T_{\text{(Curie)}}$ and $E_{\text{dc}} = 1.11$ eV above $T_{\text{(Curie)}}$. Finding practically same values apparently implies a single conduction mechanism [36]. However, the

fact that more than one conduction mechanism is expected [36] from the observed (Figure 2) “departure of the real permittivity data from a low frequency plateau-like behaviour towards the lowest frequencies and high temperature” has also been pointed out by these authors, with the comment that “further measurements and data treatment to better elucidate this additional low-frequency effect are in progress.” This motivated us (i) to use τ_{cross} to find σ_{dc} and E_{dc} , and also (ii) to try three segment fitting (Figure 18) as needed for the data resulting from the τ_{cross} -based analysis. The data actually demands a middle segment (here 570°C to 600°C) fit.

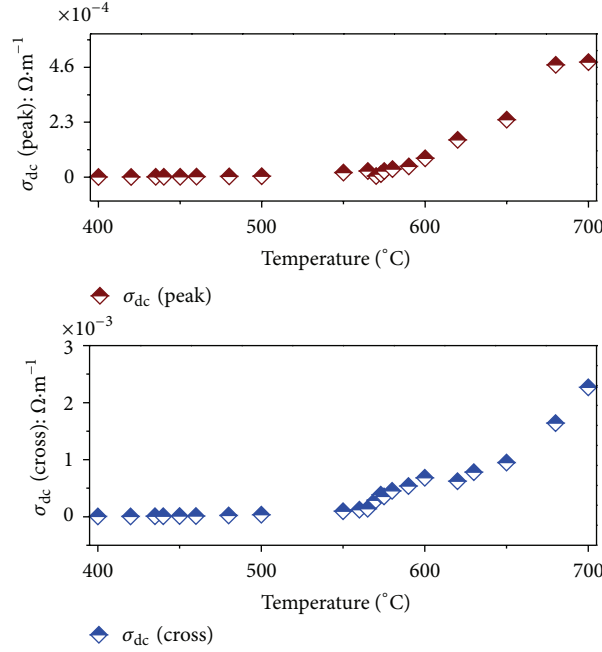


FIGURE 17: Variation of DC conductivity, $\sigma_{dc}(\text{cross/peak})$, with temperature in 400°C to 700°C range, for quenched PNO sample. Here, two values of DC conductivity, $\sigma_{dc}(\text{cross}) = (\epsilon_0 \epsilon_{\infty})/\tau_{\text{cross}}$ in the lower graph and $\sigma_{dc}(\text{peak}) = (\epsilon_0 \epsilon_{\infty})/\tau_{\text{peak}}$ in the upper graph have been calculated from τ_{cross} and τ_{peak} given in Figure 14.

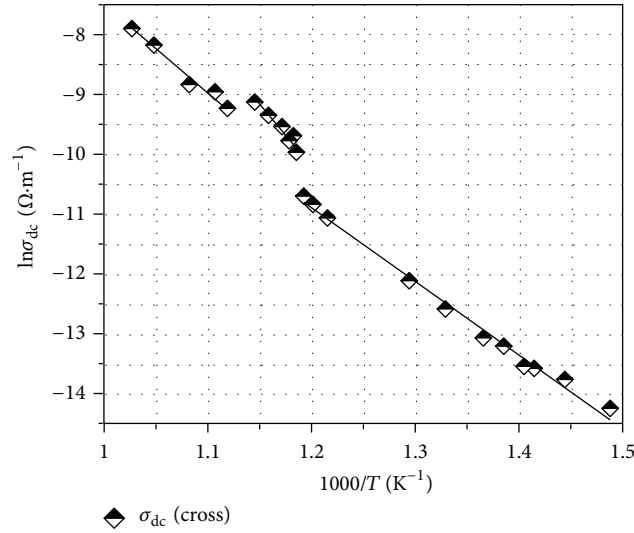


FIGURE 18: Variation of $\ln \sigma_{dc}(\text{cross})$ with $1/T(\text{K}^{-1})$ in temperature 400°C to 700°C range, and least square fitting of the liner equation in three different temperature regions that yield three different values of DC activation energy.

Here, one notes in Figure 17 that $\sigma_{dc}(\text{cross})$ versus T data clearly fall into three linear segments:

- 400°C to 565°C giving (Figure 18) $E_a = 1.0724 \pm 0.043$ eV,
- 570°C to 600°C giving (Figure 18) $E_a = 1.595 \pm 0.120$ eV,
- 610°C to 700°C giving (Figure 18) $E_a = 1.263 \pm 0.156$ eV,

which implies a peaking of the activation energy $E_a = E_{dc}(\text{cross})$ in the Curie temperature (T_c) region and practically

the same value for low and high temperature regions (“C3” data points in Figure 19). This discovers the expected [36] existence of different E_{dc} and, hence, different conduction mechanisms, retaining same or similar values of E_{dc} below and above the T_c region.

A 2-segment fit to $\sigma_{dc}(\text{cross})$ versus T data of Figure 17 yields (“C2” points in Figure 19)

$$E_a = 1.072 \pm 0.043 \text{ eV over } 400^\circ\text{C to } 565^\circ\text{C},$$

$$E_a = 1.026 \pm 0.086 \text{ eV over } 570^\circ\text{C to } 700^\circ\text{C},$$

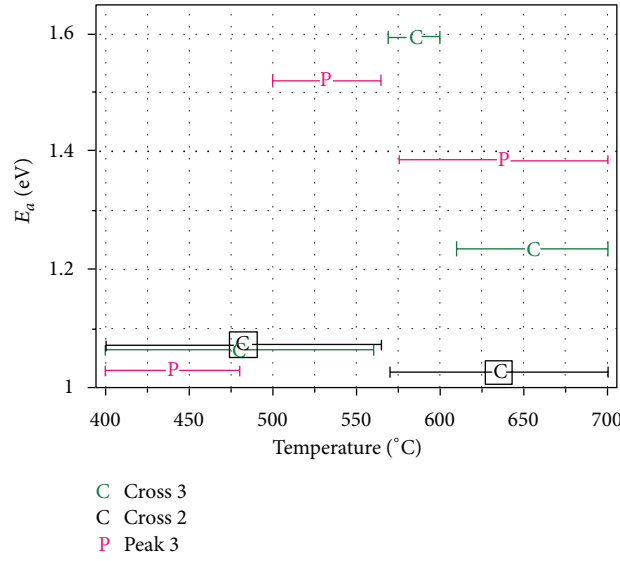


FIGURE 19: Activation energy (E_{dc}) for DC conduction in different temperature regions. P in symbol name indicates the use of peak technique of finding relaxation time, and C indicates the cross technique case. Here, 2 stands for fit to 2 temperature regions and 3 for 3 temperature regions fit, the chosen temperature region of fit being indicated by corresponding horizontal bar through the symbol.

missing the significant rise and fall within a narrow T_c region (570 to 600°C) to wrongly conclude no significant change across T_c (the Curie temperature). This is in line with the limited knowledge, currently available in the literature as already discussed.

$\sigma_{dc}(\text{peak})$ versus T data of Figure 17 can be seen to have more scatter than $\sigma_{dc}(\text{cross})$ versus T data with the former not falling well either on a set of straight lines or even on a smooth graph, as should be the case from already discussed higher scatter of τ_{peak} data. We feel that τ_{cross} should be used as relaxation time if there is a choice to choose from τ_{peak} and τ_{cross} data. Still we tried linear fits to $\sigma_{dc}(\text{peak})$ versus T data. The 3-segment fit could tackle this scattered data set relatively better as follows:

$$400^\circ\text{C to } 480^\circ\text{C } E_a = 1.028 \pm 0.101 \text{ eV,}$$

$$500^\circ\text{C to } 590^\circ\text{C } E_a = 1.523 \pm 0.130 \text{ eV,}$$

$$600^\circ\text{C to } 700^\circ\text{C } E_a = 1.387 \pm 0.168 \text{ eV,}$$

as shown in Figure 19 as “P3” data points.

So, the three-region fits of τ_{cross} and τ_{peak} suggest a peaking in E_{dc} versus T variation, at or below (resp.) the Curie temperature. This better match of the E_{dc} peak with the Curie temperature for τ_{cross} data further supports the better reliability of τ_{cross} data. Near the transition temperature, DC activation energy is highest ($1.595 \pm 0.120 \text{ eV}$), a new observation that needs further verification and explanation.

4. Conclusion

Presently prepared PbNb_2O_6 samples revealed pure orthorhombic phase by X-ray Rietveld analysis, with confirmation down to granular level, by High Resolution Transmission Electron Microscopy. These structural characterizations as well as impedance spectroscopy over 20 Hz to 5.5 MHz and up to 700°C established the high quality of these samples.

Present evaluations of DC and AC conductivities, capacitance (C) and resistance (R) of the equivalent CR circuit, relaxation times and related activation energies from the analysis of our wide-ranging impedance spectroscopy data on orthorhombic PNO, and discussions have been either more extensive than in the literature or done for the first time. This is the first reporting of the Nyquist diagram, the plot of Z'' versus Z' , for orthorhombic lead metaniobate. An impressive peak ($\sim 760 \text{ nF}$) of the equivalent CR circuit capacitance (C) in the C versus T graph has been obtained at T_m as shown. AC conductivity (σ_{ac}) is seen to peak at T_m , more prominently in the higher frequency plots. Relaxation time registers a clear peak at T_m , while falling slowly with increasing temperature in other temperature regions.

Measured DC electrical conductivity appears to show three regions of temperature dependence (Figure 17) rather than the usually tried ferroelectric and paraelectric regions. A suitably chosen transition region in the plot of $\ln(\sigma_{dc})$ versus $1/T$ in Figure 18 forms the third region, interestingly giving the highest activation energy (Figure 19). A 3-region fit should be carefully examined for different systems, since the third region may be missed due to data points, inadequate with respect to either the temperature range or the density of data points or both. Moreover, a forced two-region fit ($C2$ points in Figure 19) to data needing a three-region fit will mask the large up and down ($C3$ points) of the activation energy value in the Curie temperature region and indicate a small change of activation energy across the Curie temperature, similar to the result of 2-segment fit to time domain analysis [35] result. It appears that the DC activation energy can be estimated better from τ_{cross} and 3-segment fit (Figure 19), unless the result in a particular experiment is against 3-segment fit. Presently observed peaking of the activation energy $E_{dc}(\text{cross})$ in the Curie temperature (T_c) region is a new result.

The peak at T_m in the ϵ' versus T graph is sharp, leading to a value of ~ 1 for the diffusivity parameter and implying near absence of any relaxor property. Impedance spectroscopy showed (Table 1) highest record of ferroelectric-paraelectric transition temperature (T_m), $T_m > 580^\circ\text{C}$ for 5.5 MHz, and $T_m > 574^\circ\text{C}$ for 0.5 kHz. This implies potential use of this material for piezoelectric sensors and actuators up to temperatures much higher than the limits of BT and PZT based piezomaterials.

Acknowledgments

The dielectric measurement set-up at the Department of Ceramic Engineering, NIT, Rourkela 769008, India, has been used with the active encouragement of Professor Swadesh K Pratihari. Authors also thank Shri Pulak Ray and his team at SINP for help in TEM operation. U. De thanks Alexander von Humboldt Foundation (Germany) for partial support that led to preliminary presentation of a part of this work in international conferences and discussions.

References

- [1] I. Ihara, "Ultrasonic sensing: fundamentals and its applications to nondestructive evaluation," *Lecture Notes Electrical Engineering*, vol. 21, pp. 287–305, 2008.
- [2] R. Kazys, A. Voleisis, and B. Voleisiene, "High temperature ultrasonic transducers: review," *Ultragarsas*, vol. 63, no. 2, pp. 7–17, 2008.
- [3] G. Goodman, "Ferroelectric properties of lead metaniobate," *Journal of the American Ceramic Society*, vol. 36, no. 11, pp. 368–372, 1953.
- [4] A. A. Nesterov, E. V. Karyukov, and K. S. Masurenkov, "Synthesis of phases of composition PbNb_2O_6 and BaNb_2O_6 with the use of active precursors," *Russian Journal of Applied Chemistry*, vol. 82, no. 3, pp. 370–373, 2009.
- [5] R. S. Rath, "Unit-cell data of the lead niobate PbNb_2O_6 ," *Acta Crystallographica*, vol. 10, part 6, pp. 437–437, 1957.
- [6] U. De, "TEM, HT XRD, electrical, optical and thermal characterizations of materials for high temperature piezoelectric applications," in *Proceedings of the IUMRS-ICA*, Abstract no. 21.1078, BEXCO, Busan, Korea, 2012, <http://www.iumrs-ica2012.org/program.php>.
- [7] M. H. Francombe and B. Lewis, "Structural, dielectric and optical properties of ferroelectric leadmetaniobate," *Acta Crystallographica*, vol. 11, part 10, pp. 696–6703, 1958.
- [8] E. C. Subbarao and G. Shirane, "Nonstoichiometry and ferroelectric properties of PbNb_2O_6 -type compounds," *The Journal of Chemical Physics*, vol. 32, no. 6, pp. 1846–1851, 1960.
- [9] E. C. Subbarao, "X-ray study of phase transitions in ferroelectric PbNb_2O_6 and related materials," *Journal of the American Ceramic Society*, vol. 43, no. 9, pp. 439–442, 1960.
- [10] S. Ray, E. Günter, and H. J. Ritzhaupt-Kleissl, "Manufacturing and characterization of piezoceramic lead metaniobate PbNb_2O_6 ," *Journal of Materials Science*, vol. 35, no. 24, pp. 6221–6224, 2000.
- [11] K. R. Chakraborty, K. R. Sahu, A. De, and U. De, "Structural characterization of orthorhombic and rhombohedral lead meta-niobate samples," *Integrated Ferroelectrics*, vol. 120, no. 1, pp. 102–113, 2010.
- [12] K. R. Sahu and U. De, "Thermal characterization of piezoelectric and non-piezoelectric lead meta-niobate," *Thermochimica Acta*, vol. 490, no. 1-2, pp. 75–77, 2009.
- [13] F. Guerrero, Y. Leyet, M. Venet, J. de Los, and J. A. Eiras, "Dielectric behavior of the PbNb_2O_6 ferroelectric ceramic in the frequency range of 20 Hz to 2 GHz," *Journal of the European Ceramic Society*, vol. 27, no. 13–15, pp. 4041–4044, 2007.
- [14] S. K. Barbar and M. Roy, "Synthesis, structural, electrical, and thermal studies of $\text{Pb}_{1-x}\text{Ba}_x\text{Nb}_2\text{O}_6$ ($x = 0.0$ and 0.4) ferroelectric ceramics," *ISRN Ceramics*, vol. 2012, Article ID 710173, 5 pages, 2012.
- [15] J. W. Griffin, T. J. Peters, G. J. Posakony, H. T. Chien, and L. J. Bond, *Under-Sodium Viewing: A Review of Ultrasonic Imaging Technology for Liquid Metal Fast Reactors*, PNNL-18292, U.S. Department of Energy, Pacific Northwest National Laboratory, Richland, Wash, USA, 2009.
- [16] I. V. Kityk, M. Makowska-Janusik, M. D. Fontana, M. Aillerie, and A. Fahmi, "Influence of non-stoichiometric defects on optical properties in LiNbO_3 ," *Crystal Research and Technology*, vol. 36, no. 6, pp. 577–589, 2001.
- [17] M. Venet, A. Vendramini, F. L. Zabotto, F. D. Garcia, and J. A. Eiras, "Piezoelectric properties of undoped and titanium or barium-doped lead metaniobate ceramics," *Journal of the European Ceramic Society*, vol. 25, no. 12, pp. 2443–2446, 2005.
- [18] H. S. Lee and T. Kimura, "Effects of microstructure on the dielectric and piezoelectric properties of lead metaniobate," *Journal of the American Ceramic Society*, vol. 81, no. 12, pp. 3228–3236, 1998.
- [19] J. Soejima, K. Sato, and K. Nagata, "Preparation and characteristics of ultrasonic transducers for high temperature using PbNb_2O_6 ," *Japanese Journal of Applied Physics 1*, vol. 39, no. 5, pp. 3083–3085, 2000.
- [20] Y. M. Li, L. Cheng, X. Y. Gu, Y. P. Zhang, and R. H. Liao, "Piezoelectric and dielectric properties of PbNb_2O_6 -based piezoelectric ceramics with high Curie temperature," *Journal of Materials Processing Technology*, vol. 197, no. 1–3, pp. 170–173, 2008.
- [21] P. Q. Mantas, "Dielectric response of materials: extension to the Debye model," *Journal of the European Ceramic Society*, vol. 19, no. 12, pp. 2079–2086, 1999.
- [22] S. Zhang, C. A. Randall, and T. R. Shrout, "High Curie temperature piezocrystals in the BiScO_3 - PbTiO_3 perovskite system," *Applied Physics Letters*, vol. 83, no. 15, pp. 3150–3152, 2003.
- [23] J. R. Macdonald and W. B. Johnson, in *Impedance Spectroscopy: Theory, Experiment, and Applications*, E. Barsoukov and J. R. Macdonald, Eds., John Wiley & Sons, Hoboken, NJ, USA, 2nd edition, 2005.
- [24] S. Sen and R. N. P. Choudhary, "Impedance studies of Sr modified $\text{BaZr}_{0.5}\text{Ti}_{0.95}\text{O}_3$ ceramics," *Materials Chemistry and Physics*, vol. 87, no. 2-3, pp. 256–263, 2004.
- [25] A. Shukla, R. N. P. Choudhary, and A. K. Thakur, "Thermal, structural and complex impedance analysis of Mn^{4+} modified BaTiO_3 electroceramic," *Journal of Physics and Chemistry of Solids*, vol. 70, no. 11, pp. 1401–1407, 2009.
- [26] K. Uchino and S. Nomura, "Critical exponents of the dielectric constants in diffused phase transition crystals," *Ferroelectrics Letters Section*, vol. 44, no. 11, pp. 55–61, 1982.
- [27] L. E. Cross, "Relaxor ferroelectrics," *Ferroelectrics*, vol. 76, no. 1, pp. 241–267, 1987.

- [28] O. Raymond, R. Font, N. Suárez-Almodovar, J. Portelles, and J. M. Siqueiros, "Frequency-temperature response of ferroelectric-magnetic Pb ($\text{Fe}_{1/2}\text{Nb}_{1/2}$) O_3 ceramics obtained by different precursors—part I: structural and thermo-electrical characterization," *Journal of Applied Physics*, vol. 97, no. 8, Article ID 084107, 8 pages, 2005.
- [29] B. Behera, E. B. Arajo, R. N. Reis, and J. D. S. Guerra, "AC conductivity and impedance properties of $0.65\text{Pb}(\text{Mg}_{1/3}\text{Nb}_{2/3})\text{O}_3$ - 0.35PbTiO_3 ceramics," *Advances in Condensed Matter Physics*, vol. 2009, Article ID 361080, 6 pages, 2009.
- [30] R. N. P. Choudhary, D. K. Pradhan, G. E. Bonilla, and R. S. Katiyar, "Effect of La-substitution on structural and dielectric properties of $\text{Bi}(\text{Sc}_{1/2}\text{Fe}_{1/2})\text{O}_3$ ceramics," *Journal of Alloys and Compounds*, vol. 437, no. 1-2, pp. 220–224, 2007.
- [31] K. S. Rao, D. M. Prasad, P. M. Krishna, and J. H. Lee, "Synthesis, electrical and electromechanical properties of tungsten-bronze ceramic oxide: $\text{Pb}_{0.68}\text{K}_{0.64}\text{Nb}_2\text{O}_6$," *Physica B*, vol. 403, pp. 2079–2087, 2008.
- [32] Z. Lu, J. P. Bonnet, J. Ravez, and P. Hagenmuller, "Correlation between low frequency dielectric dispersion (LFDD) and impedance relaxation in ferroelectric ceramic $\text{Pb}_2\text{KNb}_4\text{TaO}_{15}$," *Solid State Ionics*, vol. 57, no. 3-4, pp. 235–244, 1992.
- [33] P. S. Sahoo, A. Panigrahi, S. K. Patri, and R. N. P. Choudhary, "Impedance spectroscopy of $\text{Ba}_3\text{Sr}_2\text{DyTi}_3\text{V}_7\text{O}_{30}$ ceramic," *Bulletin of Materials Science*, vol. 33, no. 2, pp. 129–134, 2010.
- [34] S. Rachna, S. M. Gupta, and S. Bhattacharyya, "Impedance analysis of $\text{Bi}_{3.25}\text{La}_{0.75}\text{Ti}_3\text{O}_{12}$ ferroelectric ceramic," *Pramana*, vol. 71, no. 3, pp. 599–610, 2008.
- [35] S. Devi and A. K. Jha, "Dielectric and complex impedance studies of $\text{BaTi}_{0.85}\text{W}_{0.15}\text{O}_{3+\delta}$ ferroelectric ceramics," *Bulletin of Materials Science*, vol. 33, no. 6, pp. 683–690, 2010.
- [36] R. L. Gonzalez, Y. Leyet, F. Guerrero et al., "Relaxation dynamics of the conductive process for PbNb_2O_6 ferroelectric ceramics in the frequency and time domain," *Journal of Physics: Condensed Matter*, vol. 19, no. 13, Article ID 136218, 2007.

